KFUPM
Journal of Undergraduate Research International

Diamond Open Access 172

Article Petroleum Engineering

Methanol Slug Sizing as a Mobility Control Strategy for Viscous Fingering Supersession in Miscible scCO2 EOR: A CMG-GEM Simulation Study

Wafa Alahmed and Sidqi Abu-khamsin*

Cite https://doi.org/10.64589/juri/221325

Submitted: November 30, 2025 **Revised:** March 17, 2026 **Accepted:** March 25, 2026

ABSTRACT

This study examined how methanol (MeOH) can improve the sweep efficiency of miscible CO_2 flooding in enhanced oil recovery (EOR) applications—a process characterized by efficient miscible oil displacement but poor areal sweep efficiency, in which the viscosity contrast between the injected and resident fluids causes CO_2 to channel through preferential paths. Vertical core flooding simulations were conducted using CMG-GEM software to evaluate the effect of MeOH slug size on displacement behavior and oil recovery at one pore volume (1 PV) injected. The analysis showed that small MeOH fractions primarily increased the supercritical CO_2 ($scCO_2$)–oil miscibility, density, and viscosity, producing only minor improvements in macroscopic sweep efficiency. By contrast, larger fractions sufficiently increased the $scCO_2$ viscosity, shifting the mobility contrast (M) to stabilize the advancing front, delay breakthrough (BT), and consolidate the $scCO_2$ channels. At sufficiently high MeOH volumes, the displacement transitioned into a near-piston-like advance with complete suppression of fingering and near-complete sweep of the core. These shifts in flow behavior increased recovery factors (RF) from approximately 73% for pure $scCO_2$ injection to nearly 99% when MeOH occupied half or more of the injected PV. Overall, the findings demonstrate that MeOH acts as both a microscopic efficiency modifier and a hydrodynamic stabilizer, with its effectiveness strongly dependent on the injected proportion. This work suggests that MeOH-assisted $scCO_2$ flooding may offer a practical pathway to improving sweep efficiency in miscible EOR processes and motivates future laboratory validation and evaluation of hybrid strategies such as water-alternating-gas (WAG) with MeOH buffering.

Keywords: CO_2 flooding, enhanced oil recovery (EOR), viscous fingering, mobility contrast, alcohol buffers, front stabilization

1. INTRODUCTION

EOR techniques are commonly required after primary and secondary mechanisms become insufficient, typically recovering only ~10% of the original oil in place (OOIP)[1] EOR strategies span thermal, chemical, and gas-injection methods, each selected based on reservoir conditions, oil properties, and operational feasibility. Among these techniques, miscible CO_2 flooding has been widely applied owing to its ability to achieve multicontact miscibility (MCM), swell the oil phase, reduce viscosity, and enhance displacement efficiency[2] When the injection pressure exceeds the minimum miscibility pressure (MMP), CO_2 diffuses rapidly into the crude oil, enriching the gas phase and lowering the interfacial tension (IFT), thereby enabling favorable flow behavior.

In miscible CO_2 flooding, viscous fingering arises owing to the injection of low-viscosity CO_2 into a considerably more viscous oil[3] When the IFT is nearly eliminated under miscible conditions, no capillary barrier exists to dampen interfacial disturbances, and any microscopic fluctuation at the CO_2–oil interface amplifies freely[4] The injected CO_2, continually driven by the pressure gradient, seeks paths of least resistance and penetrates the oil through narrow advancing channels rather than displacing it uniformly. This behavior minimizes the energy required to displace the highly viscous phase[5] As miscibility and decreasing pressure toward the outlet further reduce local resistance ahead of the front, these channels accelerate, elongate, and branch, forming the classic unstable displacement geometry known as viscous fingering[6] Extensive efforts have been made to address this challenge. Enick *et al.*[7] provided a comprehensive 40-year review of CO_2 thickeners, detailing various mobility and conformance control techniques, including WAG, surfactant-alternating-gas (SAG), foam-assisted-water-alternating-gas (FAWAG), and CO_2 flooding profile improvement. Although these methods have demonstrated efficacy in mitigating viscous fingering, the associated economic and practical constraints limit their field scale implementation. Rudyk *et al.*[8] investigated the feasibility of ethanol and MeOH as CO_2 cosolvents to enhance its molecular weight and consequently increase displacement efficiency, reporting a 19.4% increase in liquid-phase oil recovery over a pressure range of 20–60 MPa. Fang *et al*[9] employed molecular dynamics simulations to analyze the atomic-level behavior of CO_2/N_2 flooding slugs, finding

that CO_2 injected as the front slug markedly improves oil recovery owing to its high miscibility with crude oil and the propelling effect of N_2. Djabbarah[10] demonstrated that CO_2-alcohol mixtures modify MMP while increasing CO_2 density and viscosity, proposing two injection strategies: (1) premixing the chemicals before injection and (1) injecting alternating slugs of CO_2 and alcohol. Al-Azani *et al.*[11] investigated organic additives as CO_2 co-injection agents to mitigate gravity override and mobility instability during gas flooding; their experimental study on blending CO_2 with triethyl citrate demonstrated that the additive increased CO_2 viscosity and density, leading to improved sweep efficiency and reduced segregation. However, this approach has practical limitations, including the need for precise compositional control, potential phase separation under reservoir conditions, and uncertainties regarding chemical retention. Li *et al.*[12] developed a poly(vinyl acetate)-styrene (PVAc-S) polymer thickening system with ethanol as a cosolvent, reporting a 24-fold increase in CO_2 viscosity under reservoir conditions; dual-core experiments demonstrated improved mobility control, while NMR imaging confirmed a stabilized displacement front and enhanced micropore fluid mobilization. However, polymer-based thickeners may suffer from injectivity, retention, and economic limitations at the field scale.

While CO_2 EOR has been extensively studied, the use of MeOH as a discrete buffering slug in Berea sandstone has not been explored; previous studies have focused on alternative chemicals or on continuous MeOH co-injection with CO_2. MeOH is miscible with both crude oil and CO_2.[8] Furthermore, its intermediate density—falling between that of oil and $scCO_2$ (570.1 <744 <877 kg/m^3)—yields density and viscosity values more compatible with oil than CO_2, thereby supporting a stable displacement front. The increased viscosity and density of the CO_2–MeOH mixture are attributed to strong intermolecular interactions between the hydrogen-bonding groups in MeOH and the induced dipoles in CO_2. These interactions are stronger than the dispersion forces in pure CO_2, leading to (1) restricted molecular motion, which increases viscosity, and (2) stronger molecular attraction, which reduces intermolecular distance and increases mixture density.[13] This study investigated how MeOH slugs with varying PV fractions influenced BT, CO_2 mobility, displacement stability, and oil RF in vertical miscible $scCO_2$ core floods. Using a CMG-GEM simulation framework with slug fractions ranging from 1% to 90% PV, this study identified a transition from primarily improving scCO2–oil miscibility to thickening the mixture, shifting M toward hydrodynamic front stabilization at higher fractions.[4]

2. METHODOLOGY

2.1. Experimental Description. Vertical upward core flooding was simulated by injecting a MeOH pre-slug followed by $scCO_2$ for a total injection of 1 PV (Figure 1). The primary variable was the MeOH-to-CO_2 injection ratio (Table 1), evaluated in terms of CO_2 mass production behavior and RF trends. All tests were conducted under identical operating conditions.

The core model corresponded to a 30.5 cm Berea sandstone plug with a diameter of 3.78 cm; the core properties are summarized in Table 2. Berea sandstone was simulated by setting typical values for rock properties and relative permeability, as shown in Figure 2, and was selected because it is among the most common reservoir analogs in Saudi Arabia.[14] The displaced oil was Saudi Arabian light crude, and all fluid properties used in the simulations are listed in Table 3.

2.2. Simulation of Core Flooding. Core flood simulations were conducted using the CMG-GEM compositional simulator, with the model configuration illustrated in Figure 3. Fluid injection and production were imposed at a fixed rate of 0.25 cm^3/min at both the inlet and outlet to maintain steady displacement conditions. The back-pressure regulator was set to 24.132 MPa—sufficiently above the CO_2 MMP (17.24 MPa at 99 °C)[11]—to ensure single-phase miscible CO_2 flow. A confining pressure of 27.579 MPa was applied to maintain mechanical integrity and enforce upward displacement. Under these conditions, the total injection duration was 4.4 h, corresponding to 1 PV of injected fluids. These pressure and temperature conditions ensured the supercritical state of CO_2, as verified by NIST.[15]

All binary interaction coefficients were assigned a value of zero, and water saturation (S_w) was initialized at its irreducible value ($S_w = 0.20$).

3. RESULTS AND DISCUSSION

3.1. General Overview of Outcomes. The results presented in Figure 4 reveal a consistent delay in $scCO_2$ BT with increasing MeOH fraction, ultimately achieving no BT conditions at high MeOH PV fractions. This behavior reflects improvement in M, primarily through viscous thickening of the displacement front and subsequent suppression of viscous fingering.[4] In parallel, the plateau in $scCO_2$ mass production gradually diminished with increasing slug size, indicating a more uniform advancement of the displacement front.[2]

Regarding RF, Figure 5 illustrates that the RF recorded at the end of injection follows a polynomial increase with MeOH slug size before plateauing at 0.5 PV. At this plateau, RF reaches 98.95%, a marked improvement over the 73.48% recorded for the pure $scCO_2$ baseline. Collectively, these results demonstrate that MeOH buffers stabilize the displacement front, mitigate early BT, and substantially enhance the mobilization and recovery of previously trapped oil.

3.2. Initial Observations: Base $scCO_2$ Injection. The baseline simulation represented the upward injection of 1 PV of pure $scCO_2$ into a Berea sandstone core to establish a quantitative reference for subsequent co-injection runs. The $scCO_2$ mass production rate, and RF were extracted from the simulation outputs and plotted in Figures 6 and 7, respectively. These results establish a benchmark for subsequent comparisons involving MeOH-augmented floods.

As shown in Figure 6, CO_2 BT occurred at 27% PV of injected gas. The $scCO_2$ mass rate curve exhibited an exponential increase before stabilizing beyond the deviation point at 0.49 PV, where the inlet and outlet volumetric rates equilibrated at 0.25 cm^3/min. The transient growth in mass rate followed the empirical relationship developed by fitting the simulation output:

$$\dot{m}_{CO2} = 658.46PV^{11.886} \quad (1)$$

Table 1. *Sizes of MeOH slugs tested*

Case	Base Case	Case 1	Case 2	Case 3	Case 4	Case 5	Case 6	Case 7	Case 8	Case 9	Case 10	Case 11
Injection (MeOH %PV)	0%	1%	5%	10%	20%	30%	40%	50%	60%	70%	80%	90%

Table 2. *Properties of the Berea core sample*

Diameter (cm)	Length (cm)	PV (cc)	Porosity (%)	Permeability (mD)
3.79	30.48	65.33	19	260

where $\dot{m}_{CO2}$ denotes the mass production rate of $scCO_2$ and PV indicates pore volume of injected $scCO_2$.

The excellent fit of this relationship ($R^2 = 0.95$) highlights the exponential propagation of the gas front during the growth. The sharp rise near BT indicates the onset of viscous fingering, caused by the unfavorable M between the low viscosity CO_2 and the displaced oil. In this regime, localized gas intrusions penetrate the oil phase through preferential pore pathways, allowing a fraction of $scCO_2$ to reach the outlet prematurely while the remaining injected gas continued to mobilize oil within the core [5] This behavior reflects a hydrodynamically unstable yet thermodynamically consistent displacement, in which early gas arrival does not necessarily imply poor miscible sweep but rather an unstable front.

The corresponding recovery trend in Figure 7 shows an oil RF of 28.88% at BT, followed by a gradual increase to 73.48% RF at 1 PV injected. The inflection point at 0.49 PV in Figure 7 aligns with the $scCO_2$ mass rate deviation in Figure 6; both signal a shift in the governing mobility regime. Before BT, the displacement was relatively stable and dominated by limited gas mobility. After BT, continued $scCO_2$ injection increased its saturation (SCO_2) and relative permeability (k_rCO_2), thereby amplifying M and promoting fingering extension. Despite the observed instability, the front advanced uniformly with no evidence of gravity override. The consistent distribution of $scCO_2$ across the core and the absence of CO_2 accumulation at the top layer (Figure 8) confirm this behavior, attributed to the small vertical dimensions of the core and the water-wet rock characteristics.

The evolution of M before and after BT can be expressed as follows:

$$M = \frac{KrCO2@S_{avg,CO2BT}\,\mu_o}{Kro@S_{wi}\,\mu_{CO2}}, Before\ BT \tag{2}$$

$$M = \frac{KrCO2@S_{CO2,2}\,\mu_o}{Kro@S_{wi}\,\mu_{CO2}}, After\ BT \tag{3}$$

where M denotes the mobility ratio, $S_{avg,CO2BT}$ denotes the $scCO_2$ average saturation at BT, K_{ro} denotes the oil relative permeability, and μ_{CO2} denotes the $scCO_2$ viscosity.

The increase in M after BT marks the hydrodynamic shift from a frontal displacement regime to a fingered flow regime. The overall displacement efficiency continued to rise but at a diminishing rate as $scCO_2$ occupied the most conductive pore channels, leaving residual oil in less accessible regions.

This baseline behavior forms a reference framework for evaluating MeOH-assisted injections. In this context, MeOH acted as an intermediate cosolvent that temporarily bridges the $scCO_2$

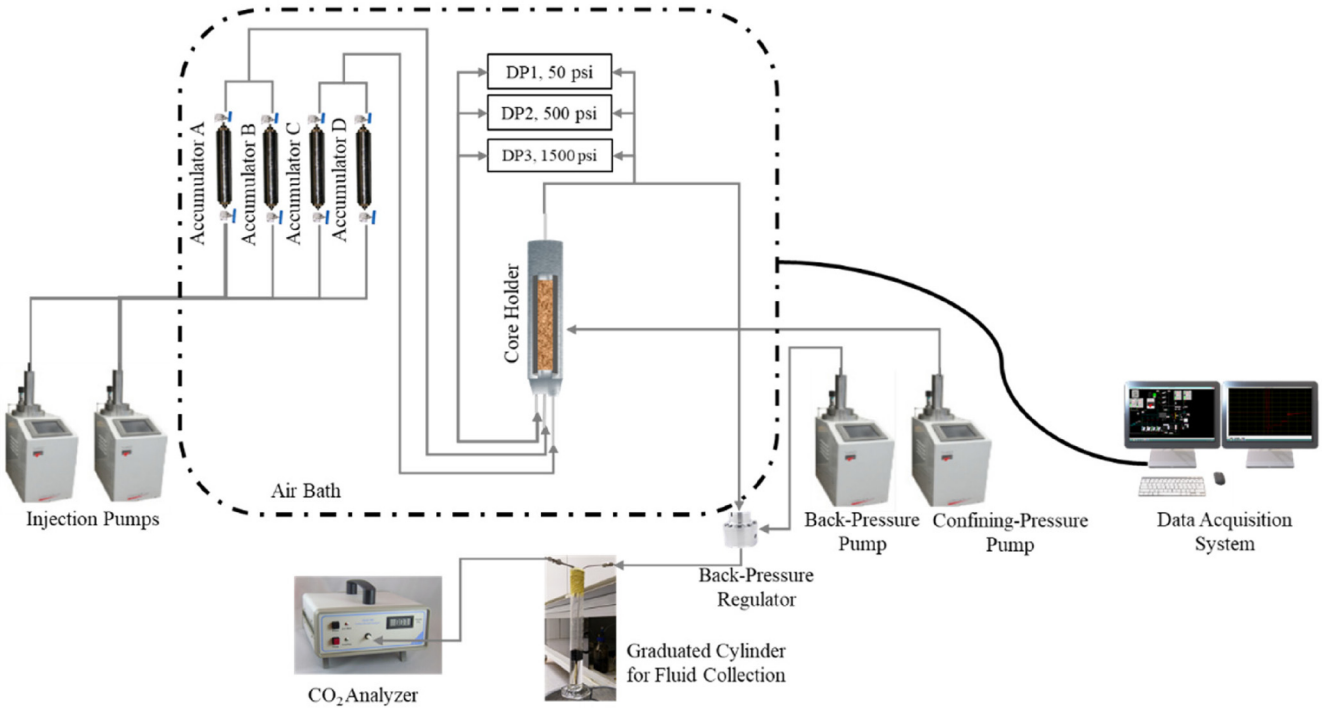

Figure 1. Schematic of experimental setup [11]

Table 3. *Properties of the fluids used in the simulation*

Fluid/Property	Critical Pressure (MPa)	Critical Temperature (K)	Density (kg/m^3)	Normal Boiling Point (K)
MeOH	8.01	512.5	744	337.8
Crude oil	1.3	960	877	810.9
$scCO_2$	7.40	300	570.1	255.4

and oil phases, introducing both thermodynamic and hydrodynamic benefits. Initially, MeOH created a transition zone that reduced the interfacial tension and increased solubility, while thickening the front through higher viscosity and density[4] As the injection progressed, $scCO_2$ dissolved into the MeOH-rich region, gradually shortening its stabilizing window and diluting the buffer. This displacement reflected the transient coupling of miscibility enhancement and CO_2 thickening. Once M reached a favorable range, hydrodynamic stabilization of the front geometry occurred, delaying BT, improving sweep, and increasing RF compared to pure $scCO_2$.

3.3. Parametric Analysis of MeOH Buffer Sizes.

3.3.1. $scCO_2$ mass production rate. The $scCO_2$ mass production behavior for all MeOH-buffered scenarios can be interpreted using Darcy's law, expressed as follows:

$$\dot{m}_{CO2} = \rho \frac{kAk_{rCO2}}{L\mu_{CO2}} \Delta P \tag{4}$$

where k_{rCO2} denotes the relative permeability of $scCO_2$, A denotes the cross-sectional area of the core, L denotes the core length, ΔP denotes the differential pressure. As k, A, L, and ΔP remain constant across all cases, the trend in Figure 4 ultimately reduces to the outlet mobility term:

$$\dot{m}_{CO2} \propto \frac{k_{rCO2}}{\mu_{CO2}} \tag{5}$$

The expected trend is consistent with intermolecular force (IMF) theory: the IMFs of the front strengthen as MeOH content increases, driven by enhanced dipole-induced dipole interactions. These interactions reduce intermolecular spacing and increase resistance to flow, thereby raising mixture viscosity and density. As the density increases, the dispersion forces responsible for improved microscopic efficiency and solubility with oil increases. Viscosity is also expected to increase throughout; however, its impact on unifying the front geometry will become apparent only after a favorable viscosity ratio between phases is achieved.[4,13] This threshold is the factor that gives IFT dominance in controlling flow geometry at low MeOH fractions, before M assumes its role in consolidating channels through sufficient thickening at higher fractions[4]

As shown in Figure 4 and quantified in Table 4, the BT timing for the low-slug cases (1%, 5%, 10%, and 20% MeOH) remained unchanged relative to the 100% $scCO_2$ base case, with BT values confined to the narrow range of 0.264–0.276 PV. This minimal deviation confirmed that low MeOH fractions provided negligible hydrodynamic stabilization to the advancing front. To achieve effective stabilization, the cumulative viscosity of the displacing fluid must be at least 30% of the oil viscosity[4] The slight smoothing observed in the CO_2 mass rate curves for these cases in Figure 4 therefore originates from thermodynamic effects—namely the modest increase in $scCO_2$ viscosity and its enhanced dissolution capacity—rather than from improved sweep control. In practical terms, 1–20% MeOH slugs alter fluid properties but not flow geometry, leaving BT essentially governed by viscous instability rather than buffer-driven mobility control. The final

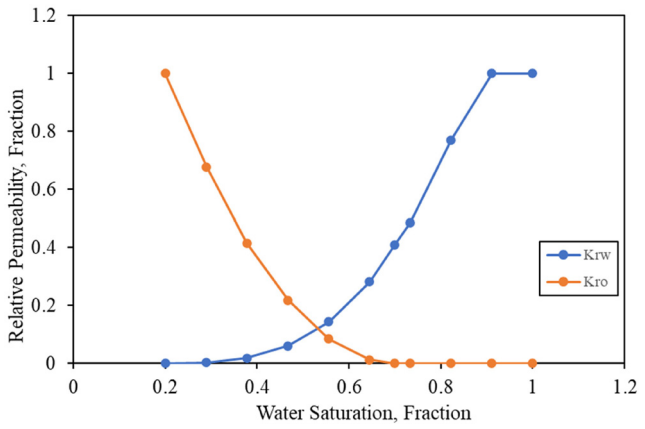

Figure 2. Relative permeability of the simulated system with water as the base permeability

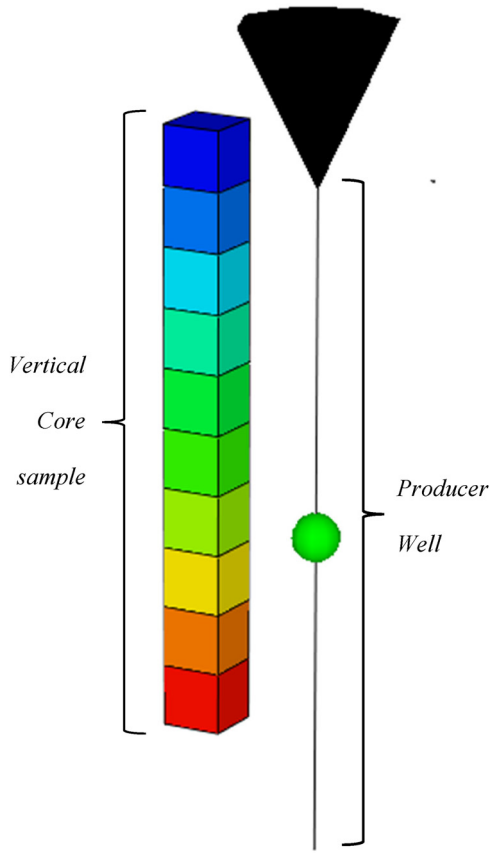

Figure 3. Simulated core flooding setup

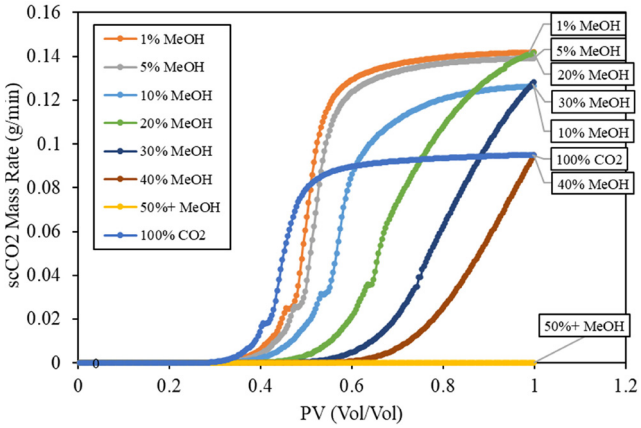

Figure 4. $scCO_2$ mass production rate over time, as simulated by CMG-GEM

CO_2 mass production rate decreased progressively with increasing MeOH proportion (0.141–0.126 g/min), further confirming the dominance of viscosity increase in Eq. (4). The trend begins to shift at the 0.2 PV MeOH slug, where the final CO_2 mass rate recovers to 0.142 g/min, indicating the first hydrodynamic contribution of MeOH. At this slug size, MeOH begins to partially stabilize the displacement front, consolidating CO_2 flow into thicker and better-connected pathways, which increases the

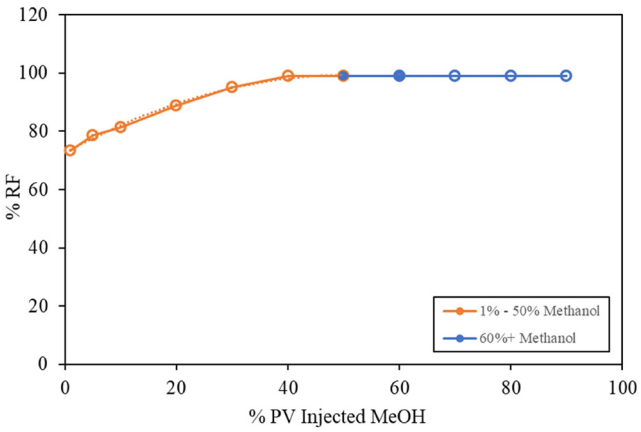

Figure 5. Final RF trend with different MeOH PV fractions

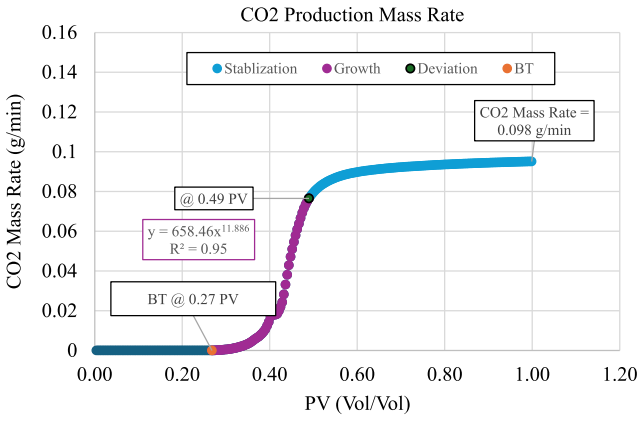

Figure 6. $scCO_2$ mass production rate behavior for 1 PV $scCO_2$ injection

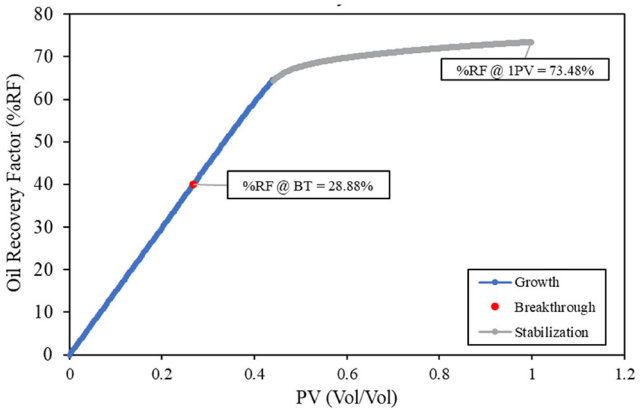

Figure 7. RF for 1 PV $scCO_2$ injection

effective gas relative permeability at the outlet and enhances the produced CO_2 mass.

A closer inspection of the final CO_2 mass production rates in Table 4 reveals an important nuance within the low-slug regime. Although the BT timing remains unchanged, the final mass rates for 1%, 5%, and 10% MeOH (0.141, 0.139, and 0.127 g/min, respectively) are all higher than the 100% CO_2 base case (0.0951 g/min). This confirms that even trace additions of MeOH sufficiently increased CO_2 viscosity and solvency, as predicted from IMF behavior[13] These enhancements raised the CO_2 mobility ($k_r,CO_2/\mu CO_2$) at the outlet without altering the flow geometry, as evidenced by the negligible variation in BT values (0.2640 to 0.2755 PV). The subsequent decline in the final $scCO_2$ mass rate from 5% to 10% MeOH reflects the growing thickening effect—$scCO_2$ viscosity increases more rapidly than relative permeability rises, causing the mobility term to weaken.

The first deviation from this thermodynamic pattern appears at 20% MeOH, where the final CO_2 mass rate climbs again to 0.142 g/min. This rebound signals the earliest onset of hydrodynamic influence: MeOH is now sufficiently voluminous to begin linking and consolidating the CO_2 micro-fingers into thicker, more coherent flow channels, increasing k_{rCO_2} at the outlet. Although this hydrodynamic contribution is still weak and insufficient to delay BT, it is strong enough to counterbalance the viscosity increase and raise the final mass rate—an effect that later evolves into the smoother curves and delayed BT observed

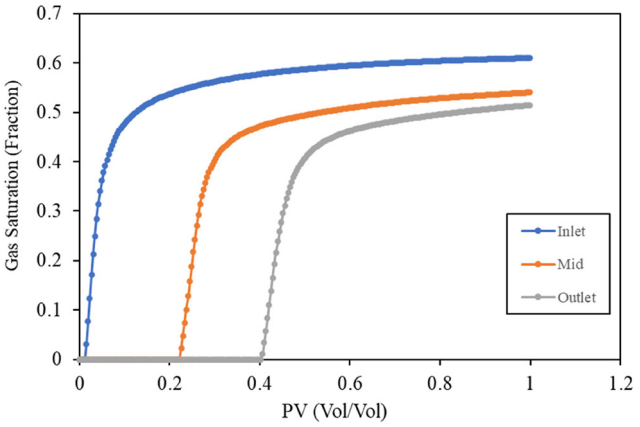

Figure 8. $scCO_2$ saturation distribution across the core sample during 1 PV flooding

Table 4. *Mass production rate and BT values for cases*

Case	Base Case	Case 1	Case 2	Case 3	Case 4	Case 5	Case 6	Case 7	Case 9	Case 10	Case 11
BT (PV)	0.268	0.272	0.276	0.264	0.264	0.279	0.364	0.448	NA	NA	NA
$\dot{m}_{CO_2}$ @ BT (g/min)	$1.01^{*}10^{-5}$	$5.04 * 10^{-6}$	$6.61 * 10^{-7}$	$2.16 * 10^{-6}$	$1.05 * 10^{-8}$	$1.17 * 10^{-15}$	$1.40 * 10^{-14}$	$3.59 * 10^{-14}$	NA	NA	NA
$\dot{m}_{CO_2}$ @ 1 PV (g/min)	0.095	0.141	0.139	0.127	0.142	0.129	0.098	0.066	NA	NA	NA

for the 30%–50% cases. Beyond this point, the dual mechanism emerges: thermodynamic thickening reduces $scCO_2$ mobility, while hydrodynamic stabilization unifies the gas front, producing the characteristic declining final mass rates and increasingly piston-like displacement observed at higher slug fractions.

The influence of hydrodynamic stabilization is also reflected in the final CO_2 mass production rates, which decrease consistently with increasing MeOH proportion, dropping from 0.129 g/min (30% PV) to 0.098 g/min (40% PV) and 0.066 g/min (50% PV). Although the buffer delays BT, it simultaneously reduces the volume of pore space immediately accessible to free CO_2, as a larger portion of the core is occupied by the MeOH-rich zone. Combined with the suppression of channeling, this leads to lower gas saturation at the outlet within 1 PV, thereby reducing k_{rCO_2} in accordance with Eq. (4). Consequently, despite the enhanced sweep efficiency, the reduction in the effective gas mobility leads to a more rapid decline in the mass production rate as slug size increases.

Collectively, the 30%–50% PV range constitutes the first regime in which MeOH exerts a dominant hydrodynamic role. In this range, the increased hydrogen-bonding density drives the viscosity and M toward a stable sweep, and the displacement front is effectively stabilized, resulting in delayed BT at the outlet. This region marks the transition from a fingering-controlled displacement to a buffered, mobility-regulated front, which becomes increasingly piston-like as the MeOH fraction increases.

The trends observed in the moderate-slug regime (30%–50% PV) continue and become fully pronounced, as the MeOH fraction increases into the 70%–90% PV range. All cases exceeding 50% PV MeOH exhibited no CO_2 BT within 1 PV of injection, signaling a complete transformation in the displacement regime. At this point, the MeOH buffer was sufficiently large to fully suppress the formation and propagation of CO_2 fingers, forcing the displacing phase to advance through a single, unified, piston-like front. This complete elimination of BT is the clearest indicator that hydrodynamic stabilization has overtaken IFT reduction, which typically amplifies fingering and now dominates sweep behavior[4, 5]

Consistently, the CO_2 mass production rates for 70%–90% PV slugs diminished further, approaching zero within 1 PV. This continued decline originates from the same dual mechanism observed at 30%–50% PV, but amplified by the much larger buffer volume: (1) most of the core pore space was occupied by the MeOH-rich zone, leaving minimal volume available for free CO_2 to mobilize to the outlet, and (2) the strong suppression of channeling markedly reduced S_{CO_2}, lowering k_{CO_2} in accordance with Eq. (5). Even though the front advanced more uniformly, the MeOH barrier blocked $scCO_2$ from reaching the outlet within 1 PV, causing the mass rate to collapse toward zero.

Overall, the 50%–90% MeOH regime represents the fully developed buffered-displacement state: the CO_2 front became entirely stabilized, BT was eliminated, channeling was fully suppressed, and outlet gas mobility dropped to negligible values. This marks the ultimate stage of MeOH-driven mobility control, where thermodynamic thickening of the gas phase and hydrodynamic front stabilization combine to produce a near-perfect piston-like sweep.

3.3.2. Oil recovery factor. The impact of MeOH on oil RF can be interpreted alongside the front-stability framework by examining Figure 9 and Table 5. All RF curves were identical up to 100% $scCO_2$ BT, where differences initially emerged through modifications in solubility, followed by changes in the local mobility regime and sweep efficiency once the cumulative mixing and compositional changes reached a threshold.

For the low-slug cases (1%, 5%, and 10% MeOH), BT, PV and RF at BT remained nearly unchanged (~40%) relative to the 100% CO_2 base case, confirming that these small slugs did not yet stabilize the front hydrodynamically. However, the final RF values at 1 PV were consistently higher than those of the base case. The base $scCO_2$ flood recovered by approximately 73.5%, whereas the 1%–10% MeOH floods yielded increasing RF values from 78.1% to 81.4%. This recovery increase occurred because MeOH mixed with CO_2 and enhanced miscibility throughout the core by strengthening the molecular attraction between the injection fluid and the oil, thereby increasing the solvency of the CO_2–MeOH phase and enabling extraction of additional oil after BT, even though the front geometry remained fingering-dominated.

At 20% MeOH, the behavior began to transition. BT PV remained close to the earlier cases; however, the RF curve in Figure 9 departed earlier from the base case after BT and climbed more steeply, reaching 88% recovery. At this stage, MeOH both

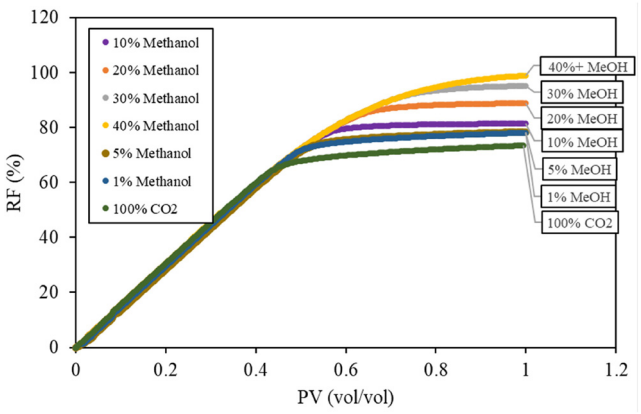

Figure 9. Oil RF curves for MeOH slugs at 1 PV

Table 5. *Oil RF values for all simulated MeOH slug cases*

Case	Base Case	1% MeOH	5% MeOH	10% MeOH	20% MeOH	30% MeOH	40% MeOH	50% MeOH	70% MeOH	80% MeOH	90% MeOH
%RF @ BT (%)	40.0263	40.7478	41.3138	39.6178	39.6699	41.9805	54.3789	65.9451	NA	NA	NA
%RF@ 1 PV (%)	73.4826	78.1448	78.4799	81.4392	88.8100	95.1744	98.9100	98.9762	98.9762	98.9762	98.9762

enhanced miscibility and increased molecular association within the mixture[13] The longer buffer slightly reduced the effective M and encouraged $scCO_2$ to flow through more continuous, better-connected pathways, increasing the post-BT recovery slope.

For intermediate slugs (30%, 40%, and 50% MeOH), the hydrodynamic contribution became much more evident. In addition to the shift of BT to a higher PV, the RF curves diverged into increasingly steeper recovery profiles after BT. The longer MeOH buffers maintained separation between the oil-MeOH and $scCO_2$-MeOH regions for longer, enhancing the properties of $scCO_2$ discussed above and increasing the contact period of the thicker MeOH layer with oil, further suppressing fingering[16] Final RF rose markedly into the mid-90% range, with the 50% slug reaching approximately 98.9%. In this regime, MeOH acted through a clear dual mechanism: enhancing miscibility while simultaneously stabilizing the front hydrodynamically, improving volumetric sweep and late-time recovery.

For the largest slugs (70%, 80%, and 90% MeOH), the behavior approached a fully stabilized limit. There was effectively no $scCO_2$ BT within 1 PV, and the RF curves approached a plateau close to the maximum RF (~99%). The MeOH zone was now sufficiently long to enforce a nearly piston-like advance while achieving maximum miscibility enhancement.

3.3.3. Interpreting MeOH-scCO₂ front behavior through kinematic theory. To verify the proposed evolution of flow behavior across the MeOH–CO_2 injection scenarios, the results were examined through the theoretical framework established by Bischofberger *et al*[4] They performed controlled miscible displacements in a Hele–Shaw geometry, injecting a low-viscosity fluid into a higher viscosity one under conditions of vanishing interfacial tension. By systematically varying the viscosity ratio while maintaining IFT near zero, they directly visualized the evolution of finger morphologies—from highly ramified, rapidly branching structures at unfavorable M, to slowed, uniform, non-branching behavior characteristic of proportionate growth as M approached unity.

Their findings demonstrated that miscible viscous fingering evolves through three distinct regimes: (1) a fingering-dominated regime, (2) a proportionate growth transition regime, and (3) a fully stabilized regime, in which the interface advances as a coherent front. The initial stage is governed by the characteristic wavelength (λ) of the most unstable mode—the physical spacing between the adjacent advancing fingers—until the M value reaches a threshold that allows the front to begin stabilizing. This description mirrors the transition observed when MeOH sufficiently altered $scCO_2$ viscosity to initiate the hydrodynamic effect.

According to classical Saffman–Taylor theory, λ decreases as M becomes increasingly unfavorable, and in the limit of vanishing IFT, the dispersion relationship predicts:

$$\lambda \propto \sqrt{\frac{\sigma}{\mu o - \mu CO_2}} \tag{6}$$

where σ denotes the IFT, μ_o and μ_{CO_2} denote the viscosities of oil and $scCO_2$, respectively. This suggests a continued reduction in λ value when a low-viscosity fluid invades a higher viscosity one ($\mu_{CO_2} \ll \mu_o$) under miscible conditions, deteriorating displacement stability as the system produces increasingly finer and more branching fingers. This behavior is consistent with the base case $scCO_2$ flood and the small MeOH slugs (1%–10%), where thin channels dominate owing to increased miscibility and thus reduced IFT, while a favorable mobility contrast has not yet been achieved. This explains the occurrence of slightly earlier BT (0.2641 PV at 20% MeOH <0.2679 PV for the base case, Table 4) and the exponential growth characteristics of the mass rate curves.

Bischofberger *et al.*[4] further demonstrated that IFT suppression alone does not determine stability. Even at IFT approaching zero, miscible flows underwent a sharp transition once the viscosity ratio μ_{CO_2}/μ_o fell within the range 0.69–1.0. In this range, the displacement entered proportionate growth: a mode in which fingers thickened, ceased branching, and advanced at comparable velocities, so that channels no longer multiply but instead grew uniformly. This theoretical shift explains the behavior observed once MeOH reached ~0.2 PV, as the viscosity of the $scCO_2$-rich phase increased sufficiently to shift M toward the proportionate growth domain. As a result, the reduction in the $(\mu_o - \mu_{CO_2})$ term began to dominate over the IFT contribution to λ, signaling the onset of increased spacing between adjacent fingers and hence more consolidated channel flow. In parallel, the final $scCO_2$ mass rate rebounded to 0.142 g/min, reinforcing the onset of channel thickening and increased connectivity—precisely the behavior predicted by the Bischofberger *et al.* framework at the onset of proportionate growth.

When MeOH reached 30%–50% PV, M improvement became dominant, and the system entered the proportionate growth transition regime. $scCO_2$ channels consolidated into fewer, wider structures, delaying BT substantially and producing the smoother, less branched mass rate trends characteristic of proportionate growth.

Finally, at 70%–90% MeOH, the system entered the fully stabilized regime: λ became large, fingers merged into a single coherent structure, and the displacement approached piston-like behavior. The simulation results—no BT, negligible $scCO_2$ mass at 1 PV, and nearly uniform oil sweep (~99% RF)—mirror the theoretical kinematic predictions with striking fidelity.

This study thus verified the transitions and microscopic physical mechanisms underlying the macroscopic behavior observed

in the simulations: the system progressed from Saffman–Taylor-dominated fingering to piston-like flooding, adhering to the kinematic theory framework.

4. CONCLUSIONS

This study quantified how MeOH–CO_2 slug sizing governs displacement stability, $scCO_2$ mobility, and ultimate RF in vertical miscible core flooding. The results showed a clear progression from fingering-dominated flow to a fully stabilized piston-like advance as the MeOH fraction increased. The effect of MeOH addition on increasing $scCO_2$ density, viscosity, and miscibility with oil aligns with the expected increase in IMFs, while the behavioral transition in front geometry can be accurately described through the Saffman–Taylor kinematic framework. The following key conclusions were drawn.

- For low MeOH slugs (1%–20% PV), BT remained unchanged (0.264–0.276 PV vs. 0.268 PV base case), confirming the absence of hydrodynamic stabilization. The $scCO_2$ mass rate at 1 PV increased slightly (0.127–0.142 g/min vs. 0.095 g/min) owing to reduced IFT and subsequently enhanced k_{rCO_2} rather than a change in flow geometry. RF improved only marginally (73%–78%), indicating that miscibility increased but sweep efficiency did not.
- The 30%–50% PV range marked the onset of hydrodynamic influence: BT shifted to 0.28–0.44 PV, reflecting partial suppression of fingering and the formation of thicker, more coherent $scCO_2$ pathways. The final $scCO_2$ mass rate decreased considerably (0.129 → 0.098 → 0.066 g/min), reflecting lower outlet gas saturation as sweep improved. RF increased sharply, rising from ∼88% at 20% PV to ∼98%–99% at 50% PV, demonstrating a transition toward piston-like advance.
- For high MeOH slugs (≥70% PV), no $scCO_2$ BT occurred within 1 PV, indicating full front stabilization and complete suppression of channeling. The mass production approached zero because most of the PV was occupied by MeOH, leaving minimal free gas near the outlet. RF plateaued at ~99%, confirming that the sweep was essentially complete and that MeOH fractions beyond 50% PV did not contribute meaningful incremental recovery.

Overall, MeOH is an effective mobility control agent whose stabilizing ability scales with injected volume. Low-range slugs influence fluid properties only, mid-range slugs begin reshaping flow geometry, and high-range slugs impose full hydrodynamic control, with ultimate RF corresponding directly to these regime shifts. Laboratory core flooding experiments are recommended to validate the alignment of the simulated trends with $scCO_2$-MeOH flooding behavior. The assumptions of zero binary interaction coefficients and the neglect of capillary effects in the pores restrict the reliability of upscaling the results, further emphasizing the need for laboratory validation of results. Additionally, hybrid buffering strategies—such as MeOH-assisted WAG—should be explored to mitigate fingering at low MeOH fractions and improve sweep without requiring large solvent volumes. To extend these findings to reservoir-scale applications, the environmental and economic feasibility of MeOH-assisted $scCO_2$ flooding should be evaluated.

AFFILIATIONS AND AUTHOR DETAILS

Undergraduate Author

Wafa Alahmed – *Department of Petroleum Engineering, King Fahd University of Petroleum & Minerals, Dhahran 31261, Saudi Arabia*; 0009-0002-2638-7728
Email: wafaalahmed00@gmail.com

Corresponding Author

Sidqi Abu-khamsin – *Research Advisor, Professor, Department of Petroleum Engineering, King Fahd University of Petroleum & Minerals, Dhahran 31261, Saudi Arabia*; 0000-0001-7047-025X
Email: sidqi50@gmail.com

ACKNOWLEDGMENTS

The authors acknowledge the support provided by the Department of Petroleum Engineering and the Undergraduate Research Department at King Fahd University of Petroleum and Minerals, particularly Dr. Shabeeb Alajmi for supervising the final stages of the paper development and Mr. Mohamed Abdalla for his technical support in the CMG simulation conduct. The authors also acknowledge the Department of Petroleum Engineering at the Colorado School of Mines for providing access to the CMG software, with special thanks to Dr. Yu-Shu Wu and Ishraq Aldarwish. The authors acknowledge Computer Modelling Group Ltd. for granting access to the CMG-GEM simulator and Salman Alrasheed for his feedback on the manuscript.

REFERENCES

(1) U.S. Department of Energy. Enhanced Oil Recovery. https://www.energy.gov/fecm/enhanced-oil-recovery.

(2) Abunumah, O., Ogunlude, P. & Gobina, E. Experimental Evaluation of the Mobility Profile of Enhanced Oil Recovery Gases. *Advances in Chemical Engineering and Science,* **11**, 154–164 (2021).

(3) Qingwang, Y., Bowen, L. & Aryana, S. New phase diagram of miscible viscous fingering instabilities in porous media with dead-end pores. *Physics of Fluids,* **34**, 092109 (2022).

(4) Bischofberger, I., Ramachandran, R. & Nagel, S. R. Fingering versus stability in the limit of zero interfacial tension. *Nat Commun* **5**, 5265 (2014).

(5) *Why Honey Makes These Strange Tendrils.* (2025) https://youtu.be/VdwSMytC7y4?si=XjNV9pKDzEXR77VT.

(6) Dorota, A. & Wojciech, P. Band Deformation in Non-Isocratic Liquid Chromatography. Band deformation in non-isocratic liquid chromatography. *TrAC Trends Anal. Chem.* **81**, 69–78 (2016).

(7) Enick, R., Olsen, D., Ammer, J. & Schuller, W. Mobility and Conformance Control for CO2 EOR via Thickeners, Foams, and Gels - A Literature Review of 40 Years of Research and Pilot Tests. *SPE Improved Oil Recovery Symposium* SPE-154122-MS (2012).

(8) Rudyk, S., Hussain, S. & Spirov, P. Supercritical extraction of crude oil by methanol- and ethanol-modified carbon dioxide. *J. Supercrit. Fluids* **78**, 63–69 (2013).

(9) Feng, L.-C., Cheng, K.-W., Tang, M. & Chen, Y.-P. Vapor–liquid equilibria of carbon dioxide with ethyl benzoate, diethyl succinate and isoamyl acetate binary mixtures at elevated pressures. *J. Supercrit. Fluids* **21**, 111–121 (2001).

(10) Djabbarah, N. Miscible Oil Recovery Factor Using Carbon Dioxide and Alcohol.*US patent*, US4899817A, (1988).

(11) Al-Azzani, K., Abu-Khamsin, S. & Sultan, A. Experimental Study of Blending CO2 with Triethyl Citrate for Mitigating Gravity Override During Reservoir Flooding. https://doi.org/10.1007/s13369-020-04901-z (2020) doi:https://doi.org/10.1007/s13369-020-04901-z.

(12) Li, L. *et al.* Performance Evaluation of a Novel CO2 Flooding Thickening System for Low-Permeability Reservoirs and an Experimental Study on Enhanced Oil Recovery. *Arab J Sci Eng* **46**, 6787–6796 (2021)

(13) Burke, J. Solubility Parameters: Theory and Application. https://cool.culturalheritage.org/coolaic/sg/bpg/annual/v03/bp03-04.html (1984).

(14) Haertmann, J. & Moosdorf, N. The new global lithological map database GLiM: A representation of rock properties at the Earth surface. **13**, 1–37 (2027).

(15) NIST. Isothermal Properties for Carbon dioxide. (2025).

(16) Craft, B. C. & Hawkins, M. *Applied Petroleum Reservoir Engineering*, 3rd Edition, (2014)